Summer Student Programme 2023

Short-term Internship report

TDPAC measurements in Bismuth Ferrite

Author
Danylo Kviatkovskyi (European Organization for Nuclear Research (CERN), Geneva, Switzerland and Taras Shevchenko National University of Kyiv, Kyiv, Ukraine)

Supervisors
Dr. Juliana Schell (European Organization for Nuclear Research (CERN), Geneva, Switzerland and Institute for Materials Science and Center for Nanointegration Duisburg-Essen (CENIDE), University of Duisburg-Essen, Essen, Germany)

Thien Thanh Dang (Institute for Materials Science and Center for Nanointegration Duisburg-Essen (CENIDE), University of Duisburg-Essen, Essen, Germany)

ABSTRACT

Over the past decades, multiferroic materials have attracted increasing attention due to their potential for various practical applications in technology. Multiferroic materials demonstrate more than one of the main properties of ferrous in one phase, which include ferromagnetism, ferroelectricity and ferroelasticity. In the group of materials that demonstrate these characteristics, $BiFeO_3$ (BFO) is currently the most interesting and most studied, as both its Néel and Curie temperatures are well above room temperature ($T_N \approx 370$ ºC and $T_C \approx 820$ ºC).[1,2]

That is why in this report we present a study local magnetoelectric effect at Bi site in multiferroic bismuth ferrite ($BiFeO_3$ or BFO) by using time differential perturbed angular correlation (TDPAC) spectroscopy. The main approach is to use the ^{111m}Cd (^{111}Cd) probe as a tracer ion for the investigation of the Bi site. The TDPAC measurements were carried out at various temperatures (15 – 500ºC) after thermal treatment at 800ºC in air for 20 minutes. The resulting TDPAC spectra show the absence of magnetoelectric coupling at the site of the bismuth ion in antiferromagnetic BFO below the Néel temperature. This key investigation experimentally confirms the anti-parallel alignment of iron-spins in BFO in anti-ferromagnetic (AF) phase. The experimental results agree well with calculations based on TDPAC theory. The substitutional Bi site location of the ^{111m}Cd (^{111}Cd) probe is confirmed using *ab-initio* DFT simulations.

CHAPTER 1: BFO and its properties

As we have already mentioned, bismuth ferrite is one of the most interesting multiferroics to study. A lot of previous investigators have shown that $BiFeO_3$ (BFO) exhibits both magnetism and particularly strong ferroelectricity at RT and thus might be implemented and utilized effectively in various electronic devices such as sensors, data storage, memory devices, and spintronic and photovoltaic devices. This indicates the potential for future BFO-related innovations, according to the literature.[1,3]

Multiferroics are defined as materials that exhibit more than one of the primary ferroic properties in the same phase:[4]

- ferromagnetism – a magnetisation that is switchable by an applied magnetic field;
- ferroelectricity – an electric polarisation that is switchable by an applied electric field;
- ferroelasticity – a deformation that is switchable by an applied stress.

Multiferroics are often referred to as magnetoelectric materials because they possess both magnetic and electric ordering. This unique property, known as magnetoelectric coupling, allows for the manipulation of magnetization by an electric field and vice versa. In essence, these materials offer a bridge between electric and magnetic phenomena.

Many multiferroic materials are based on the perovskite crystal structure, characterized by the chemical formula ABX_3. In this structure, 'A' represents larger cations, 'B' represents smaller cations, and 'X' represents anions. Perovskite materials can be engineered to exhibit multiferroic behavior by carefully selecting the elements occupying the 'A' and 'B' sites.[5]

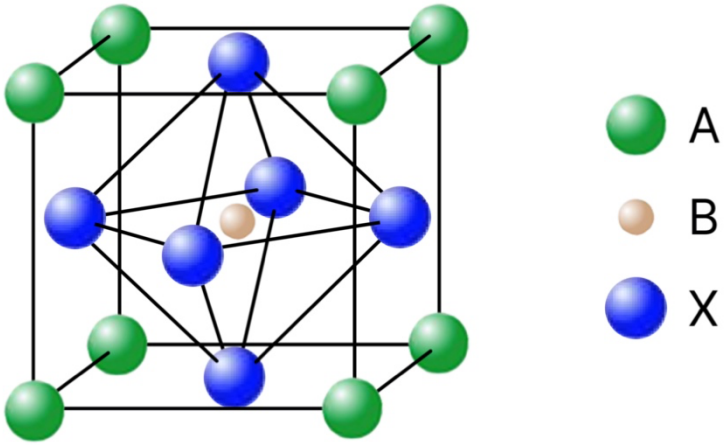

Fig. 1. Perovskite crystal structure

Figure 1 shows the visual representation of the perovskite structure, where the cations A and B are coordinated by corner linked octahedra of the X anions, and the B cation sits in the center of these octahedra, forming a three-dimensional network.

CHAPTER 2: BFO α-phase

According to the literature[1,6], the crystal structure of BFO in the α-phase is the rhombohedral *R*3*c* space group with the hexagonal cell parameters $a = 5.58$ Å and $c = 13.87$ Å at room temperature (RT). The α-phase exists up to $T_C \approx 820$°C. The stability of this phase can be divided into two nonoverlapping temperature regions, with the Néel temperature T_N as the boundary line. Below T_N, which includes RT, BFO exhibits antiferromagnetic (AFM) properties. Above T_N, and up to the Curie temperature T_C, BFO is in the paramagnetic state. Around T_C, a ferroelectric-paraelectric phase transition appears in the β phase. Before BFO undergoes this ferroelectric transition, it undergoes a large spontaneous polarization ($P \approx 90$–100 μC cm^{-2})[7,8] in the pseudocubic [111] direction, based on the work of T. T. Dang et al.[3]

Bi^{3+} and Fe^{3+} cations generate a nonconventional spontaneous electric polarization which is stabilized by the 6*s* lone pair electrons of Bi, a slight rotation of the oxygen octahedra, and a certain displacement of the iron ion. The rhombohedrally distorted perovskite structure of space group *R3c* results from 1 out of 8 possible orientations for polarization along the body diagonals of a pseudocubic unit cell; one such configuration is shown in Figure 2. Within a single ferroelectric domain, the crystal is rhombohedral with polarization along $[111]_{cubic} = [001]_{hex}$. Below the Néel temperature, the magnetic moments of the Fe^{3+} cations interact via superexchange along the Fe-O-Fe bonds at a canting angle of 156°, which leads to antiferromagnetism. On top of this local structure, the magnetic moments generate an incommensurate cycloidal structure of magnetic moments in their respective easy planes. The cycloid has propagation direction along any one $[110]_{cubic}$ crystal orientation perpendicular to the axis of electrical polarization. Both vectors span up the corresponding easy magnetic plane, based on the research by J. Schell et al.[9]

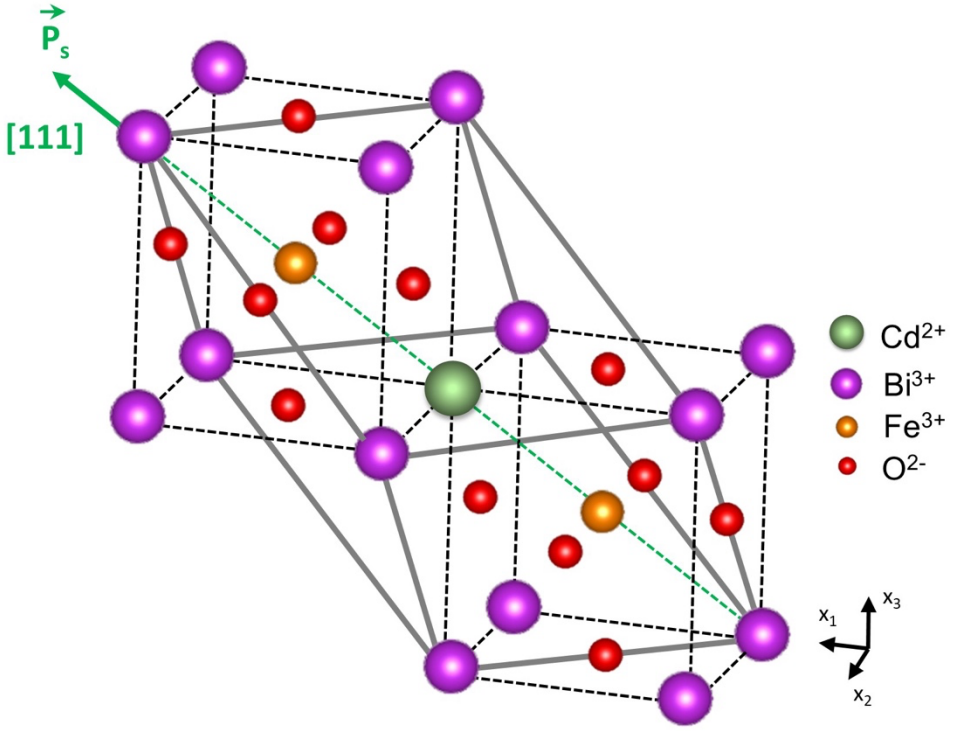

Fig. 2. The rhombohedral unit cell (formed by two-unit cell of the pseudo-cubic perovskite) of the crystal structure of $BiFeO_3$ with Bi-site substitution of Cd^{2+}. P_s indicates spontaneous electric polarization (designed by Thien Thanh Dang)

Our study limits to the α-phase, specifically antiferromagnetic phase (AF) where the measuring temperature is lower than 400°C because we would like to explore the local magnetoelectric coupling.

CHAPTER 3: TDPAC

The technique known as time differential perturbed γ-γ angular correlation, often abbreviated as TDPAC or TDPAC-Spectroscopy allows the investigation of the electromagnetic fields interacting with a nuclear probe located in the material[10, 11]. The probe nucleus, implanted in the sample, in its excited state decays to its ground state via the sensitive intermediate state through a γ-γ cascade decay. Through an angular correlation between the first and the second γ-ray, distinguished through their energies and detection times, hyperfine interactions between the probe nuclei and their surrounding atomic structure can be monitored. A fixed detector, which detects a first quantum γ_1, defines a reference axis, conventionally designated as the *z*-axis. A number of nuclei with their initial spin I_i aligned to this direction is selected. This nuclear alignment leads to an anisotropic radiation of γ_2 with regard to γ_1[12]. If the probe nucleus quadrupole momentum is disturbed through an electric field gradient (EFG) while being in the intermediate state, its spin *I* will experience a torque which forces a spin-precession around the before-referenced *z*-axis. Caused by this precession, the population of the intermediate state sublevels changes with time, which again affects the spacial anisotropy of the γ_1-γ_2 correlation. An electric field gradient is caused by charge distributions which deviate from an ideal spherically symmetric arrangement around the probe atom. It is defined as the second spacial derivative of the electrostatic potential. Through a diagonalization of the interaction Hamiltonian, rotating the tensor into its principal component coordinate system and the use of the Laplace equation, the EFG can be described by its largest component V_{zz} and the asymmetry parameter, based on the research by G. Marschick et al.:[2]

$$\eta = \frac{V_{xx} - V_{yy}}{V_{zz}} \tag{1}$$

The observable spin dependent quadrupole frequency is calculated through:

$$\omega_Q = \frac{eQV_{zz}}{4I(2I-1)\hbar} \tag{2}$$

where *e* is the electron charge, *Q* the quadrupole moment of the intermediate state of the probe nucleus, *I* its angular momentum, and $\hbar$ the reduced Planck's constant.

Generally one uses the derived quantity ν_Q[9,13]:

$$\nu_Q = \frac{eQV_{zz}}{h} \qquad (3)$$

which is called the electric quadrupole interaction frequency.

For an anisotropy coefficient η of zero, the lowest detectable substate-transition frequency is:

$$\omega_1 = k\omega_Q, \qquad (4)$$

with $k = 6$ for half-integer values of spin momentum, like the $I = 5/2$ level of the probe isotope ^{111m}Cd. The higher-ordered frequencies are calculated through $\omega_n = n\omega_1$.

If η is different from zero, the transition frequencies ω_n are functions of ω_Q and η itself:

$$\omega_1 = 2\sqrt{3}\alpha\omega_q \sin\left(\frac{1}{3}\arccos(\beta)\right) \qquad (5)$$

$$\omega_2 = 2\sqrt{3}\alpha\omega_q \sin\left(\frac{1}{3}[\pi - \arccos(\beta)]\right) \qquad (6)$$

$$\omega_3 = 2\sqrt{3}\alpha\omega_q \sin\left(\frac{1}{3}[\pi + \arccos(\beta)]\right) \qquad (7)$$

with

$$\alpha = \sqrt{\frac{28(3+\eta^2)}{3}} \qquad (8)$$

and

$$\beta = \frac{80(1-\eta^2)}{\alpha^3} \qquad (9)$$

It is noted in some literatures that the observable spin dependent quadrupole frequency in (2) is expressed by ω_0, where $\omega_0 = 6\omega_Q = \frac{3\pi}{10}\nu_Q$. Therefore, it is inferred from (4) that $\omega_0 = \omega_1$(lowest detectable substate-transition frequency) when η = 0.

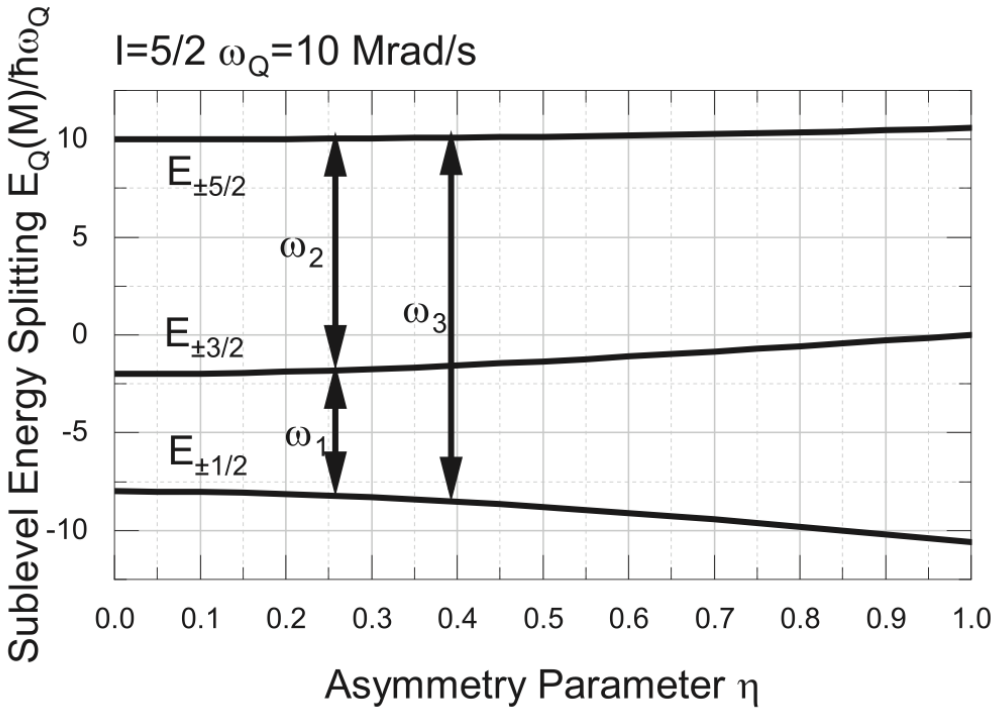

Fig. 3. Change of sublevel energies $E_Q(M)$ with increasing asymmetry parameter. Reference value only valid for I = 5/2, taken from the work of Marschick et al.[2]

When two successive γ rays are emitted from a single nucleus, they can be observed using two detectors placed in either perpendicular or opposite orientations. By exploring all potential arrangements of detector positions, both with four and six detectors, we can create 12 and 30 individual coincidence spectra, respectively. Within each of these coincidence spectra, any background noise arising from chance coincidences is subtracted. This process enables us to determine the experimental count rate ratio, denoted as R(t), which characterizes the disparity between the coincidence count rates observed when the two detectors are positioned at 180° and 90° orientations:[14]

$$R(t) = 2\frac{W(180°,t)-W(90°,t)}{W(180°,t)+2W(90°,t)} = A_{22}^{\text{eff}}G_{22}(t) \qquad (10)$$

where $W(180°, t)$ denotes the fourth or sixth root of the product of the 180° spectra after background subtraction and zero-point adjustment. Here, $W(90°, t)$ denotes the 8th or 24th root of the product of the 90° spectra from the 4- or 6-detector setups, respectively. Also, A_{22}^{eff} is the experimental anisotropy coefficient of the γ_1 -γ_2 cascade and $G_{22}(t)$ is the theoretical perturbation factor, whose form depends on the type of hyperfine interaction induced at the probe site:[3]

$$G_{22}(t) = \sum_{i=1}^{m} f_i(a_{0i} + \sum_{n=1}^{30} a_{ni}\cos(\omega_{ni}t) \cdot exp\{-0.5[(\delta_i\omega_{ni}t)^p + (\omega_{ni}\tau_R)^2]\})\exp(-\lambda_i t) \quad (11)$$

where f_i is the fraction of probe atoms exposed to the hyperfine interaction i (i = 1, 2, 3, …). ω_{ni} are transition frequencies taken from 30 nondiagonal elements of a 6×6 frequency matrix; a_{ni} are taken from 30 nondiagonal elements of a 6×6 amplitude matrix and are amplitudes of 30 corresponding transition frequencies; a_{0i} is determined from the sum of six diagonal elements of the amplitude matrix and is called the hard-core value. The values p = 1 and 2 in the exponent represent Lorentzian and Gaussian distributions respectively. δ_i is the extent of angular distortion of the local environment around the probe. τ_R is the finite time resolution (full width at half maximum) of the detectors. λ_i is the exponential decay constant or dynamic transition, according to the literature.[3]

More detailed information about TDPAC can be found in the literature.[15,16]

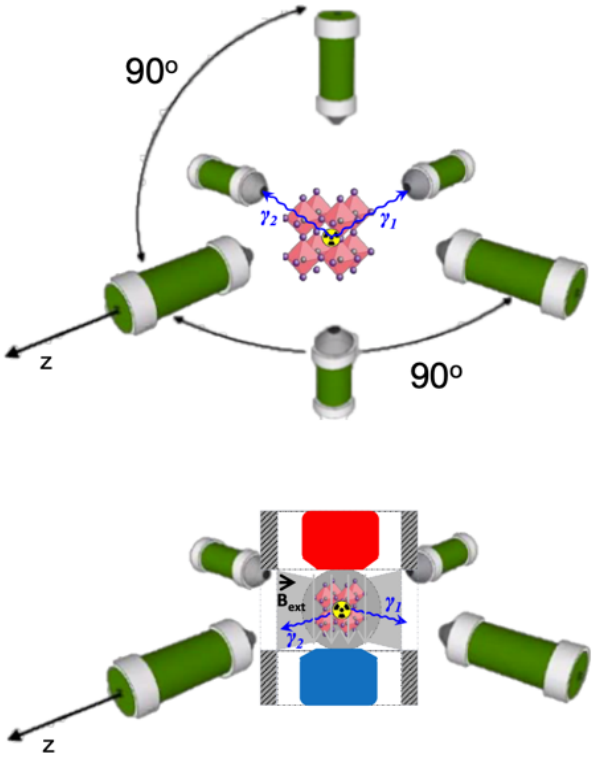

Fig. 4. Location of detectors around the sample with the radioactive probe in the experimental setup (Image by Thien Thanh Dang 2023)

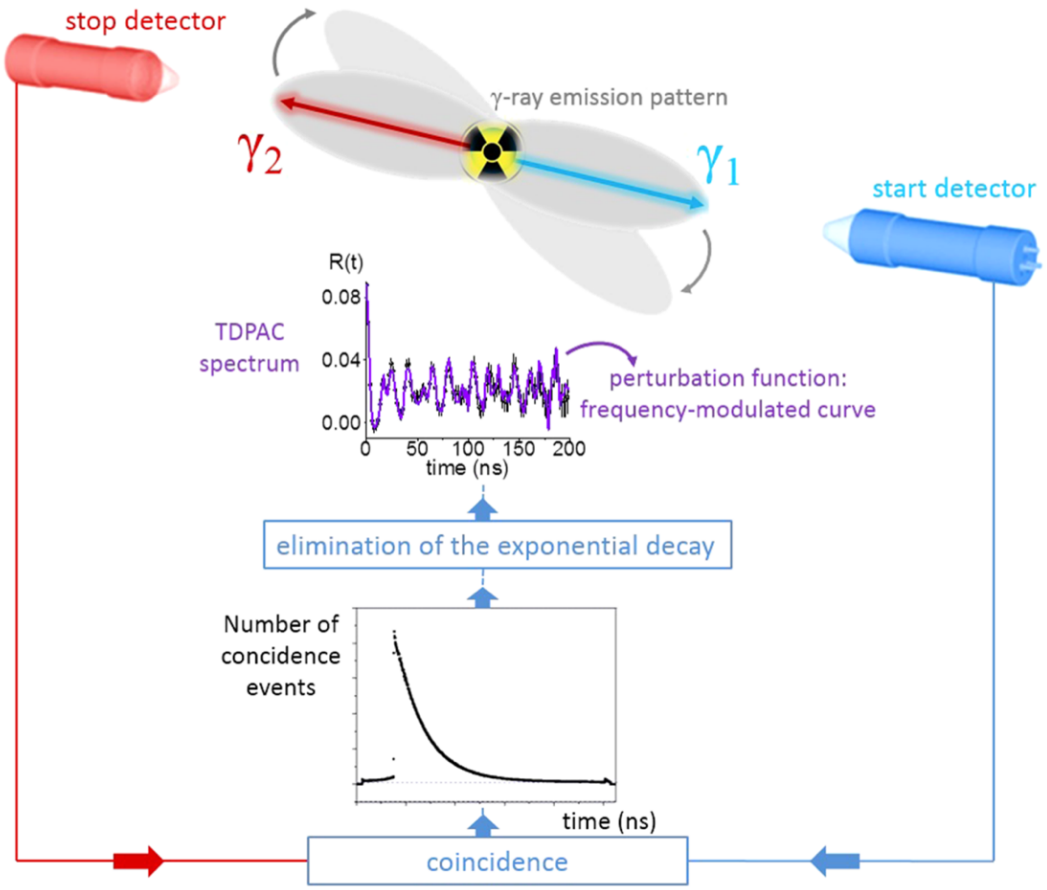

Fig. 5. Basic representation of the γ-γ TDPAC technique: detection and coincidence of the rotating emission gamma-cascade pattern, elimination of the exponential decay and generation of frequency-modulated TDPAC curve of the intermediate state, taken from literature[11]

CHAPTER 4: ^{111m}Cd probe

In this research, the nuclear probe utilized to characterize BFO bulks is ^{111m}Cd. This allows us to investigate the hyperfine interaction between this probe and the nearby atoms by utilizing the TDPAC technique.

To prepare a sample with a nuclear probe for TDPAC measurements, we used the implantation method at ISOLDE-CERN, more detailed information can be found in the literature [17,18]. During implantation, a radioactive ion beam with the energy of 30 keV is generated and directed into the crystal lattice of the sample. These ions either come to a stop at interstitial sites or push a lattice-atom out of its place and replace it. This leads to a disruption of the crystal structure, which can be investigated with TDPAC. A careful annealing procedure gradually corrects defect bonds between atoms, thereby leading to the recovery of the regular lattice structure in the local environment of the probe isotopes, based on the research of Schell et al.[19]

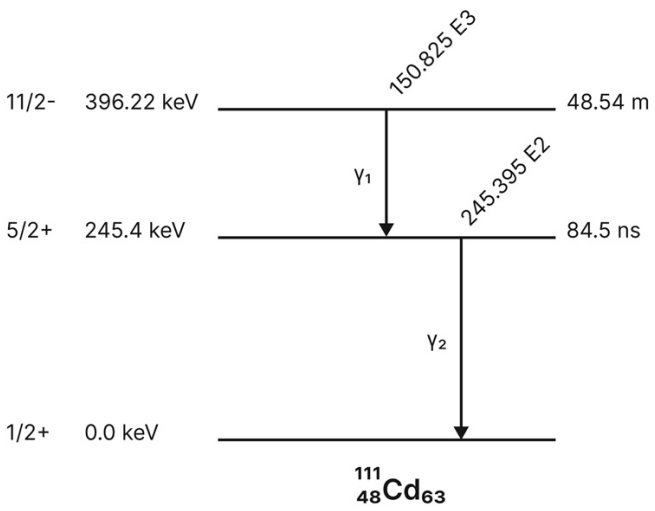

Fig. 6. Decay schema of ^{111m}Cd, data taken from the IAEA Table of Nuclides.[20]

CHAPTER 5: Data results and discussions

5.1 More about TDPAC detector and sample

Figure 7 shows two types of experimental TDPAC spectrometers at ISOLDE. First one is an analogue TDPAC setup (with 4 detectors) named K1 and second one is a digital TDPAC setup (with 6 detectors) named KATAME. A (4-/6-) detectors TDPAC-spectrometer, produces 12/30 coincidence spectra, which are not all similar. There are a set of similar spectra taken with detectors at 90 degrees and another set of spectra taken at 180 degrees. These two sets of spectra are combined to build the R(t) anisotropy ratio function, i.e., the observable containing all the information regarding the coupling of the nuclear moments with the hyperfine magnetic field and electric field gradient, according to the literature.[11] More detailed information about TDPAC spectrometers with 4- and 6-detectors can be found in literature.[11, 21]

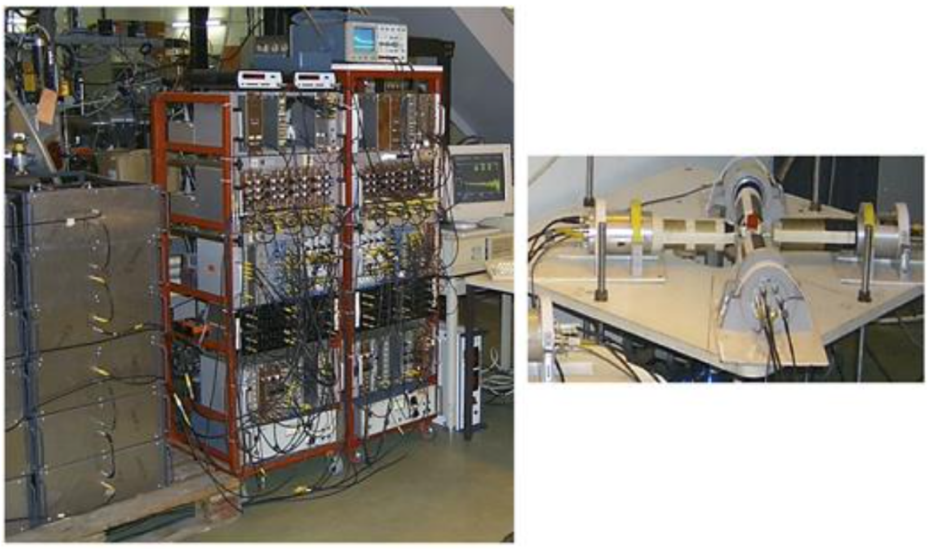

(a) (b)

(1)

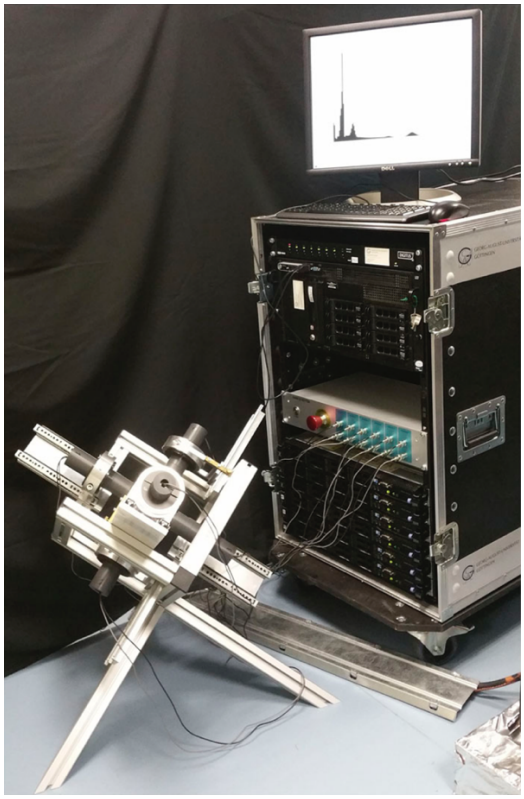

(2)

Fig. 7. Experimental TDPAC spectrometers. (1) Analogue TDPAC setup (K1) at the ISOLDE. (a) Electronic system with delay boxes; (b) the four detectors setup. (2) Digital and compact TDPAC setup (KATAME), taken from literature.[11]

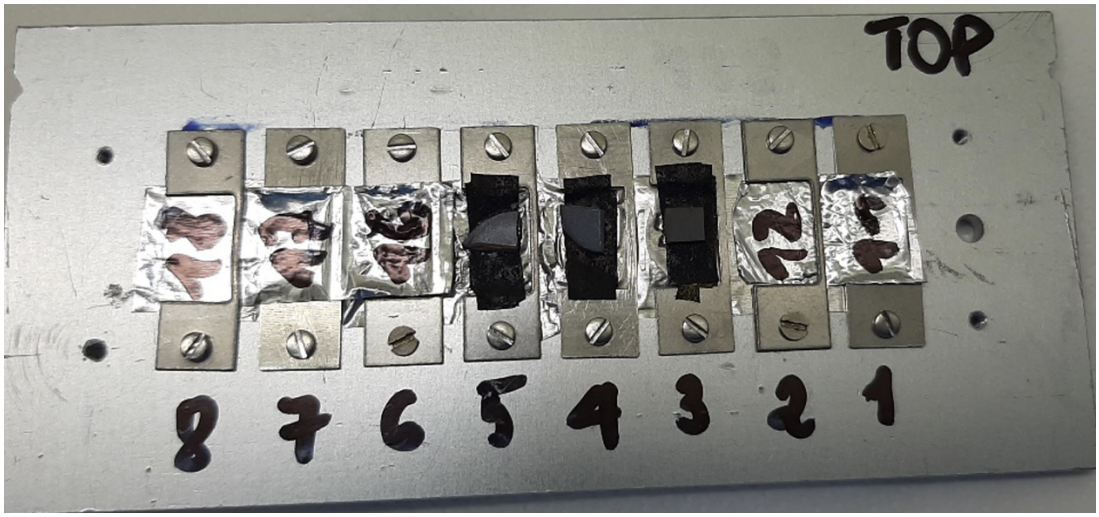

Fig. 8. BFO samples (~4×4 mm) on sample holder (positions 3, 4, 5)

5.2 Compressed method

One of the goals of this research is to compare the obtained data with the compressed data to understand how much the too fine data sampling and the compressed data differ in data fitting. And to compress the data, we can use a smoothing algorithm, where only every other output is stored, according to the literature:[22]

$$y_j \equiv y_{2k} = \frac{1}{4}(f_{k-1} + 2f_k + f_{k+1}) \qquad (12)$$

Where j = 0, …, $\frac{N}{2}$

And we assume that for y_0, $f_{-1} = f_0$. Here, there is no phase shift. The visualization of the smoothing algorithm for data compression is shown in Figure 9.

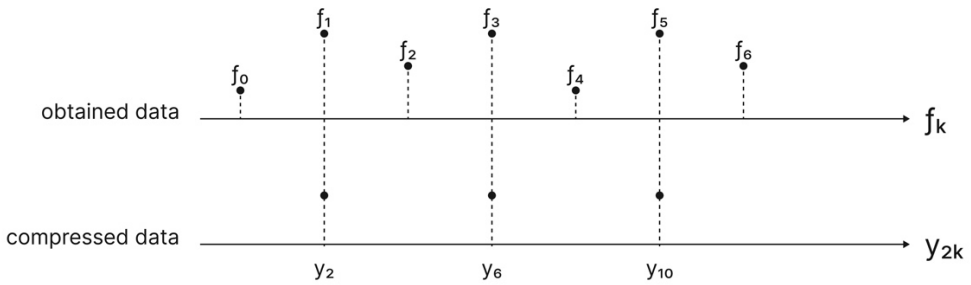

Fig. 9. Data compression algorithm

5.3 Experimental results and discussions

5.3.1 Non-compressed R(t) spectra

A. One fraction:

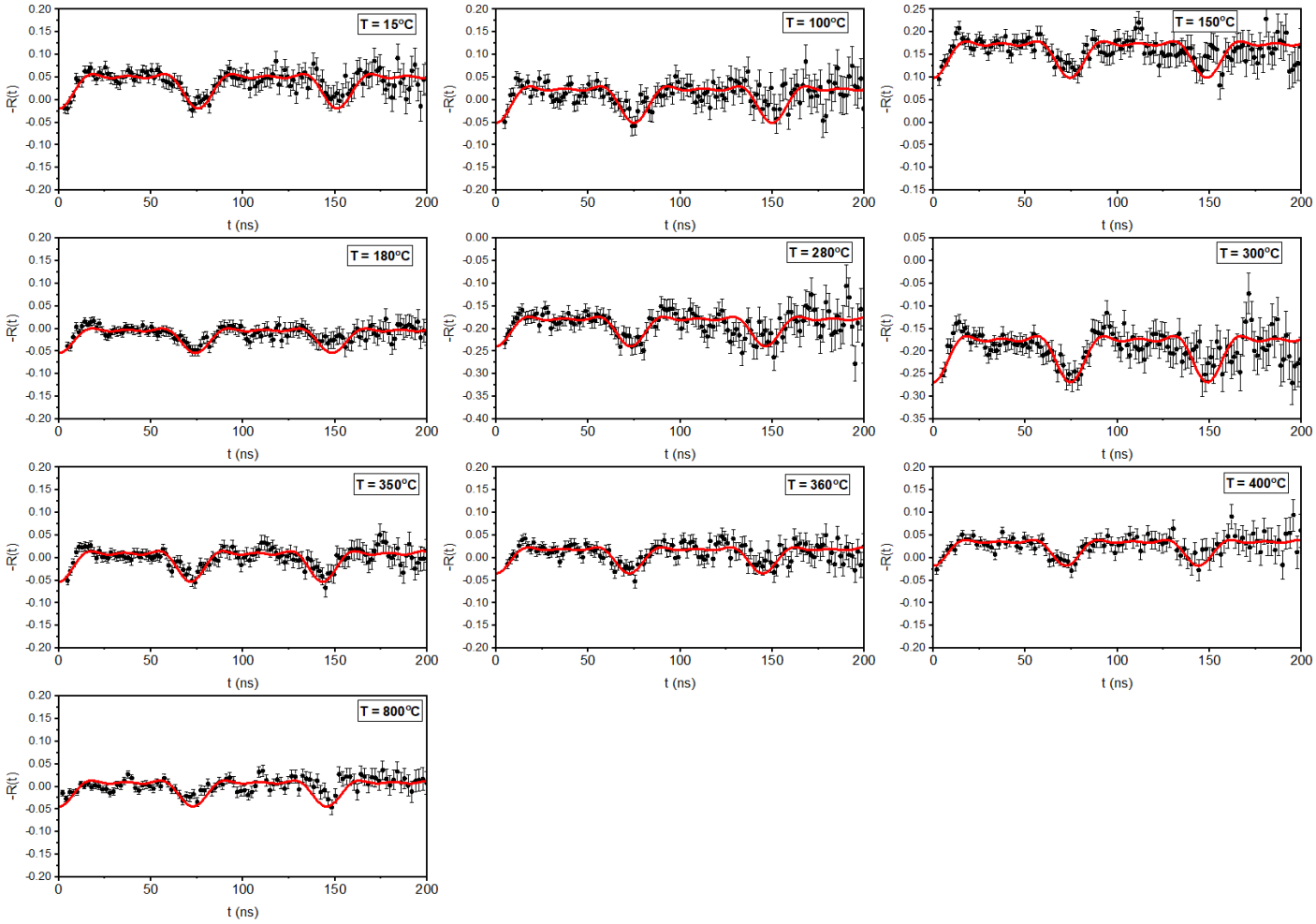

Fig. 10. Fitting curves for non-compressed spectra for one fraction

Table 1

T [°C]	f_1 [1]	ν_{Q1}, MHz	η_1[1]	δ_1[1]
15	1	88.2±0.5	0	0
100	1	88.9±0.6	0	0
150	1	89.8±0.6	0	0
180	1	89.9±0.7	0	0
280	1	91.1±0.6	0	0
300	1	89.5±0.5	0	0
350	1	93.1±0.4	0	0
360	1	92.1±0.6	0	0
400	1	92.5±0.5	0	0
800	1	91.6±0.6	0	0

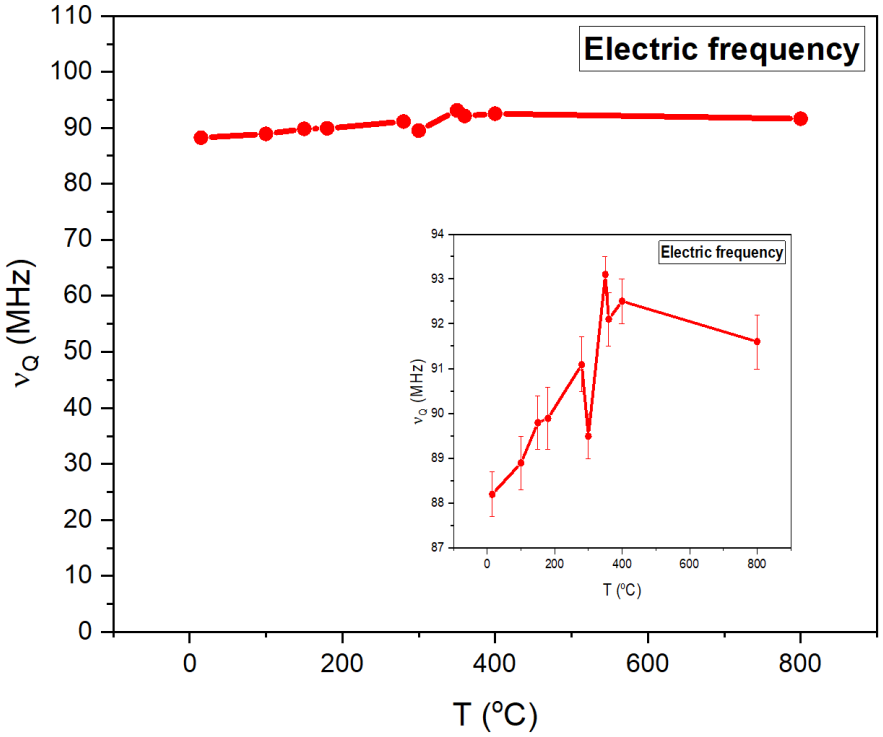

Fig. 11. Dependence of electric frequency on temperature for the one fraction case

Figure 10 shows quite unsuccessful and inaccurate fit, especially at high temperature region (T > 280ºC), with only one fraction. This can be seen in the first 25 nanoseconds, when the fitting curve does not match the experimental data. For this reason, all spectra will be refitted with two fractions.

B. Two fractions:

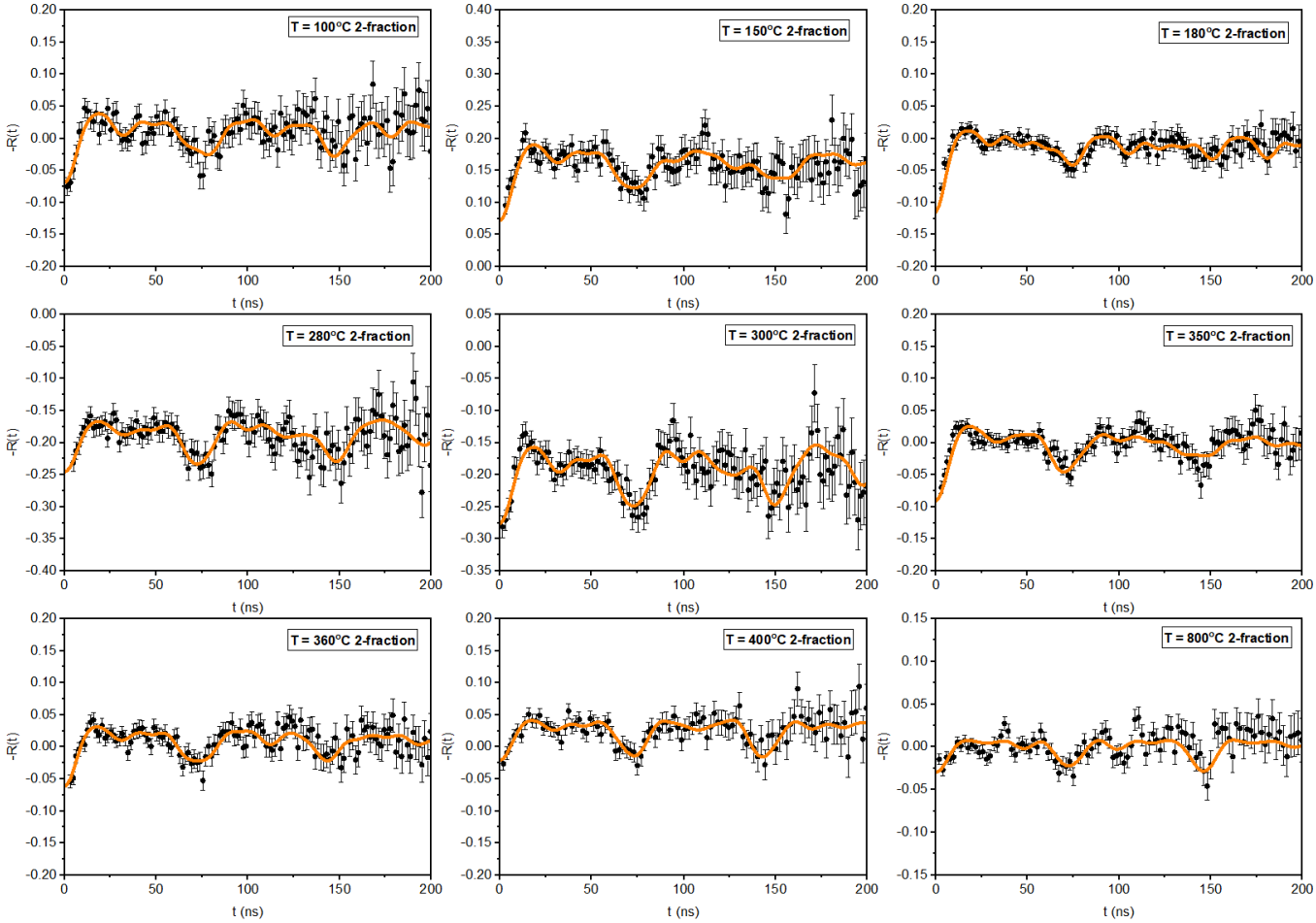

Fig. 12. Fitting curves for non-compressed spectra for two fractions

Table 2

T [°C]	f_1 [1]	f_2 [1]	ν_{Q_1}, MHz	ν_{Q_2}, MHz	η_1 [1]	η_2 [1]	δ_1[1]	δ_2[1]
100	0.71±0.09	0.29±0.06	86.88±1.64	123.55±1.42	0.19±0.07	0.76±0.03	0.09±0.04	0
150	0.83±0.08	0.17±0.05	87.96±1.45	120.61±2.20	0.18±0.06	0.91±0.05	0.10±0.03	0
180	0.77±0.06	0.23±0.04	91.97±1.22	137.52±1.01	0	0.59±0.02	0.17±0.03	0
280	0.79±0.07	0.20±0.07	89.38±0.74	117.06±2.86	0.21±0.03	0.89±0.05	0	0
300	0.73±0.05	0.27±0.06	88.08±0.64	118.20±1.73	0.23±0.03	0.88±0.03	0	0
350	0.84±0.08	0.16±0.05	91.15±1.92	116.02±2.29	0.18±0.06	0.87±0.03	0.14±0.03	0
360	0.79±0.06	0.21±0.04	93.51±1.47	127.46±1.43	0	0.67±0.03	0.11±0.03	0
400	0.80±0.07	0.20±0.07	92.32±0.76	131.42±2.72	0	0.70±0.06	0	0
800	0.79±0.10	0.21±0.10	91.80±0.10	134.96±3.52	0	0	0	0

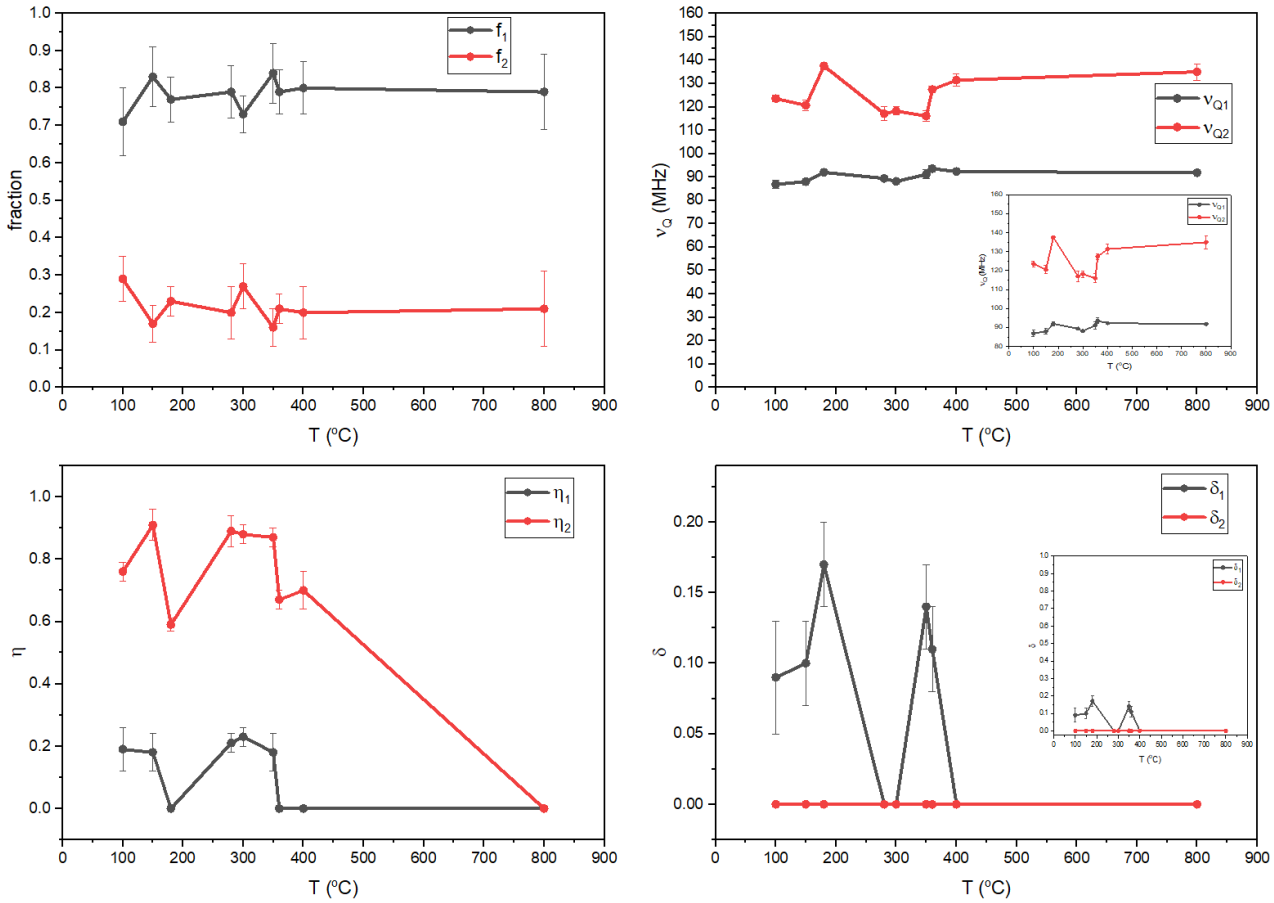

Fig. 13. Curves of hyperfine interaction parameters for two fractions

The second fraction will be necessary because part of the probe is likely to be located at Bi-site with surrounding distorted Bi atoms. While the first fraction means that Cd is located at Bi-site near a less distorted Bi atoms. Tables 2 and 4 show that the probability that the probe will be located near a less distorted Bi-atoms is greater (first fraction f_1) than when the probe is located near a distorted Bi-atoms (second fraction f_2).

In other words, fitting with two fractions gives much better results than fitting with only one fraction, because it considers the probability that the probe can be either near a distorted Bi-site or near a less distorted one. The small percentage of distorted Bi atoms probably originates from synthesizing process (solid-state reaction approach).

As shown in Table 2 and Figure 13, the electric frequencies from both fractions behave independently with measuring temperatures although there is a

little fluctuation around 130 MHz at low temperature region for fraction 2. The electric frequency for fraction 1 is quite stable around 87 MHz, which is compatible with DFT simulation presented in the work of Marschick et al.[2]. In fact, the stoichiometric replacement of Bi^{3+} (0.103 nm)[23] with a smaller ionic radii substituent (Cd^{2+}: 0.095 nm) will decrease the lattice parameter and unit cell volume[24, 25]. In addition, the structure of $BiFeO_3$ is distorted from rhombohedral to orthorhombic. Consequently, the orthorhombic structure is more stable than that of original rhombohedral $BiFeO_3$[25, 26]. This agrees well with our TDPAC result that the electric field gradients (EFGs) behave independently with measuring temperatures. However, with low concentration of ^{111m}Cd (ppm: parts per million) the crystallography will not be changed from rhombohedral to orthorhombic as reported from literatures[24,25,26]. What we obtain here is just defect relaxation at local scale. So, in our study with ^{111m}Cd tracer the BFO structure stabilizes locally (not macroscopically).

The damping factors from both fractions are almost zero, reflecting the fact that the Cd-probe is well-situated at Bi-site, and therefore the electric frequencies are well-distributed around the mean value. This also confirms that the ion implantation process and thermal treatment after implantation were well performed.

The asymmetry parameter for fraction 1 is zero or close to zero, which is also in good agreement with the DFT simulation[2], reflecting that the charge distribution around the Cd-probe is symmetrical. The asymmetry parameter for fraction 2, in contrast, is close to 1. That means the Cd-probe is surrounded by highly asymmetrical charge due to distorted environment (Bi-atoms) as discussed above.

When we replace Bi^{3+} with Cd^{2+}, this leads to a change from Fe^{3+} to Fe^{4+} in the compound to compensate unbalanced charge, which in turn means that the magnetic moment will be close to zero for Fe^{4+} ions, and therefore no magnetic frequency will be observed, based on the work of Zhou et al.[27] The existence of Fe^{4+} in the unit cell shown in Fig. 2 will break down the super exchange interaction between Fe^{3+}-Fe^{3+} which is known as the main mechanism leading to anti-ferromagnetic order in bismuth ferrite $BiFeO_3$.

5.3.2 Compressed R(t) spectra

C. One fraction:

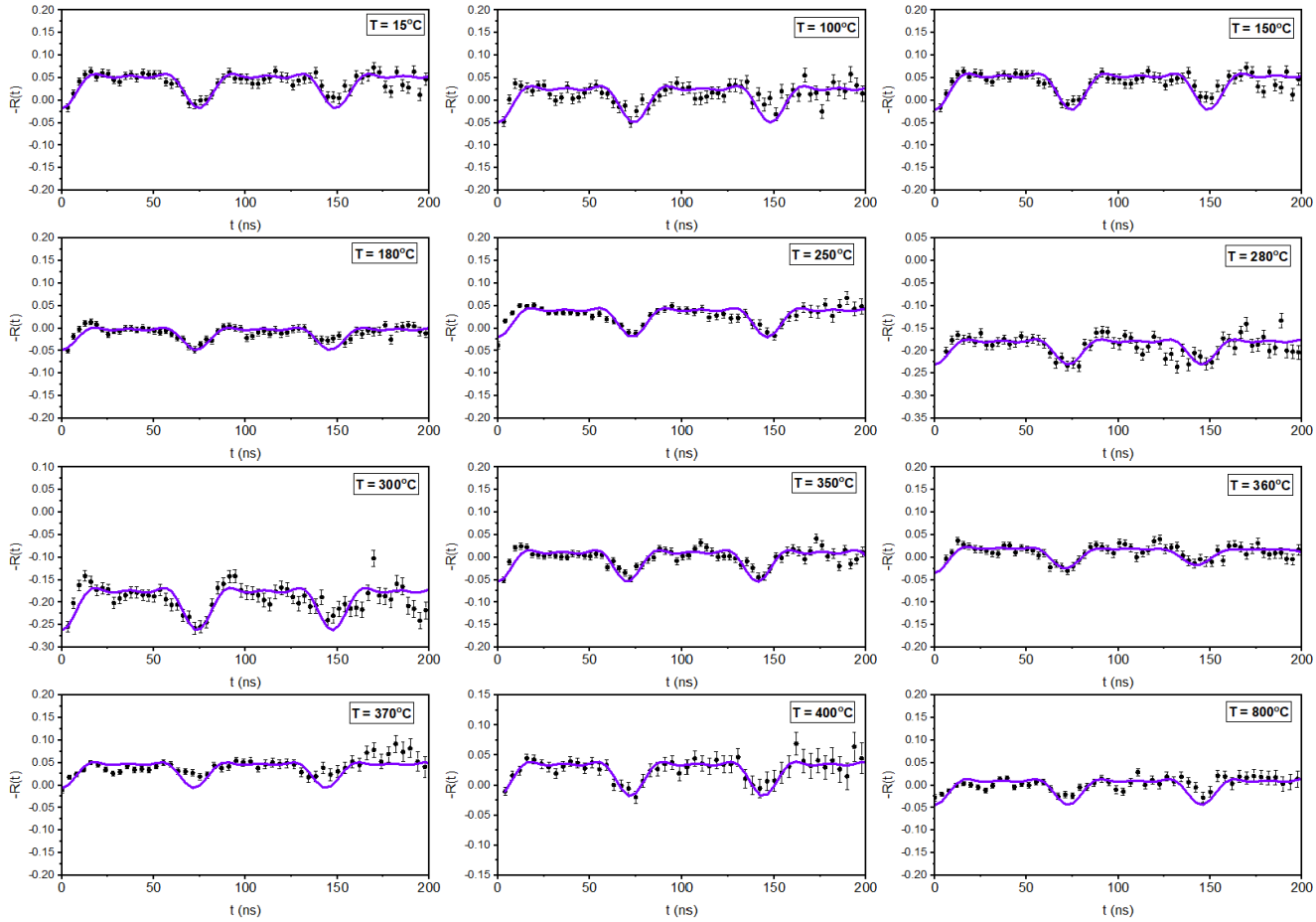

Fig. 14. Fitting curves for compressed spectra for one fraction

Table 3

T [°C]	f_1 [1]	ν_{Q1}, MHz	η_1[1]	δ_1[1]
15	1	89.5±0.4	0	0
100	1	90.1±0.7	0	0
150	1	89.5±0.4	0	0
180	1	91.3±0.5	0	0
250	1	91.2±0.6	0	0
280	1	91.6±0.9	0	0
300	1	90.5±0.7	0	0
350	1	94.5±0.5	0	0
360	1	93.5±0.7	0	0
370	1	92.7±0.9	0	0
400	1	92.5±0.5	0	0
800	1	91.7±0.8	0	0

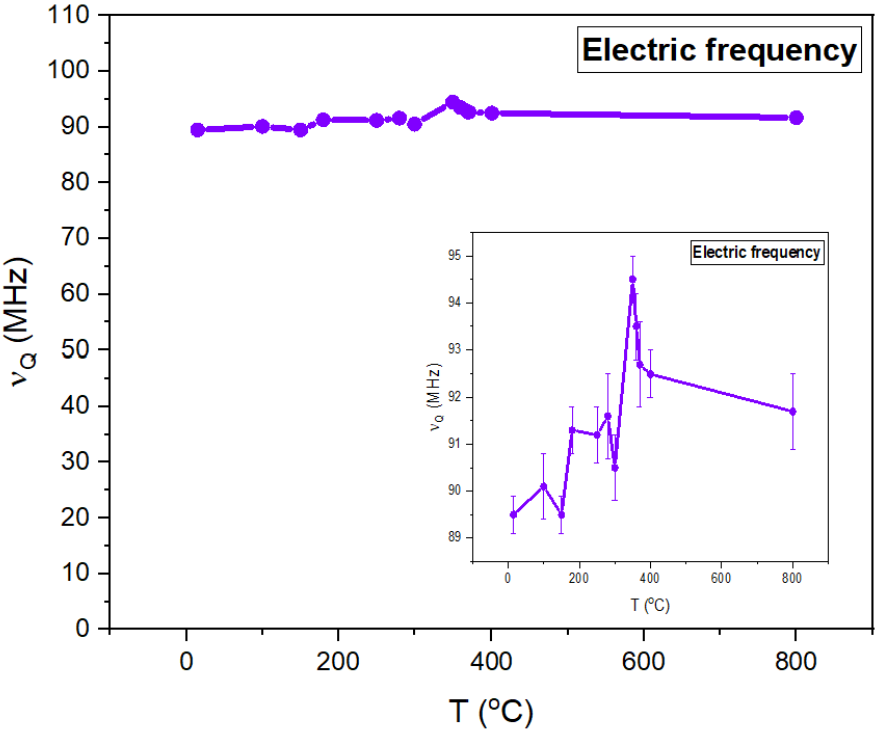

Fig. 15. Dependence of electric frequency on temperature for the one fraction case (compressed data)

D. Two fractions:

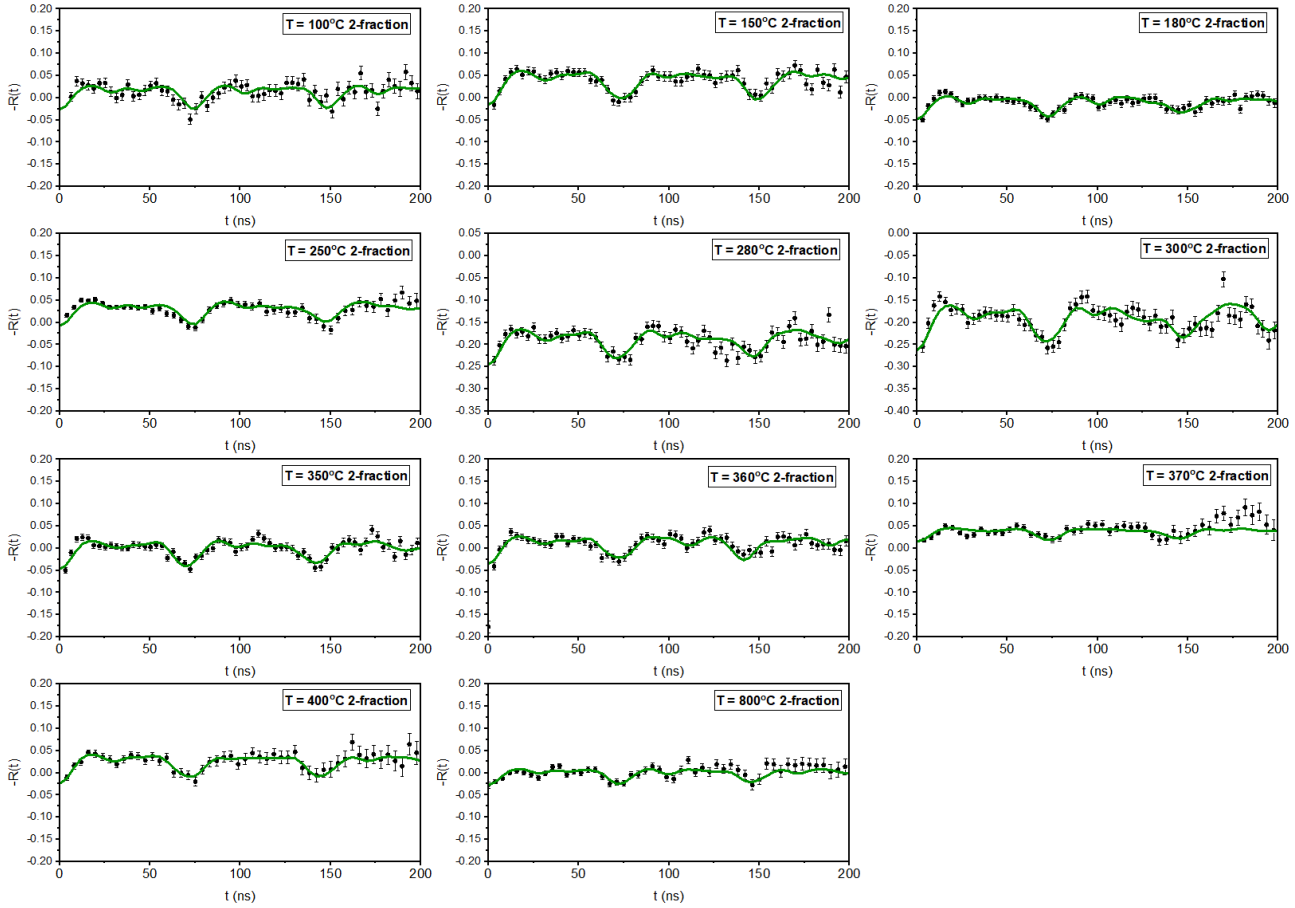

Fig. 16. Fitting curves for compressed spectra for two fractions

Table 4

T [°C]	f_1 [1]	f_2 [1]	ν_{Q_1}, MHz	ν_{Q_2}, MHz	η_1[1]	η_2[1]	δ_1[1]	δ_2[1]
100	0.71±0.15	0.29±0.15	89.37±1.35	141.28±3.16	0	0.59±0.05	0	0
150	0.78±0.06	0.22±0.07	88.98±0.59	119.71±2.10	0.12±0.04	0.87±0.03	0	0
180	0.70±0.06	0.30±0.07	91.19±0.64	140.41±1.37	0	0.71±0.02	0	0
250	0.78±0.10	0.22±0.10	90.12±0.96	137.94±3.34	0.18±0.05	0.66±0.06	0	0
280	0.73±0.15	0.27±0.11	90.59±0.94	118.69±2.75	0.20±0.04	0.88±0.04	0	0
300	0.76±0.08	0.24±0.09	89.71±0.82	117.68±2.54	0.21±0.04	0.94±0.08	0	0
350	0.82±0.08	0.18±0.09	93.10±0.77	115.98±11.91	0.16±0.04	0.98±0.42	0	0
360	0.71±0.07	0.29±0.07	94.34±0.58	130.02±1.45	0	0.62±0.03	0	0
370	0.80±0.17	0.20±0.16	91.36±1.80	107.43±6.99	0.14±0.12	0.75±0.17	0	0
400	0.83±0.06	0.17±0.06	92.35±0.61	125.33±3.25	0	0.88±0.05	0	0
800	0.73±0.11	0.27±0.12	91.26±1.41	144.20±3.63	0	0.65±0.07	0	0

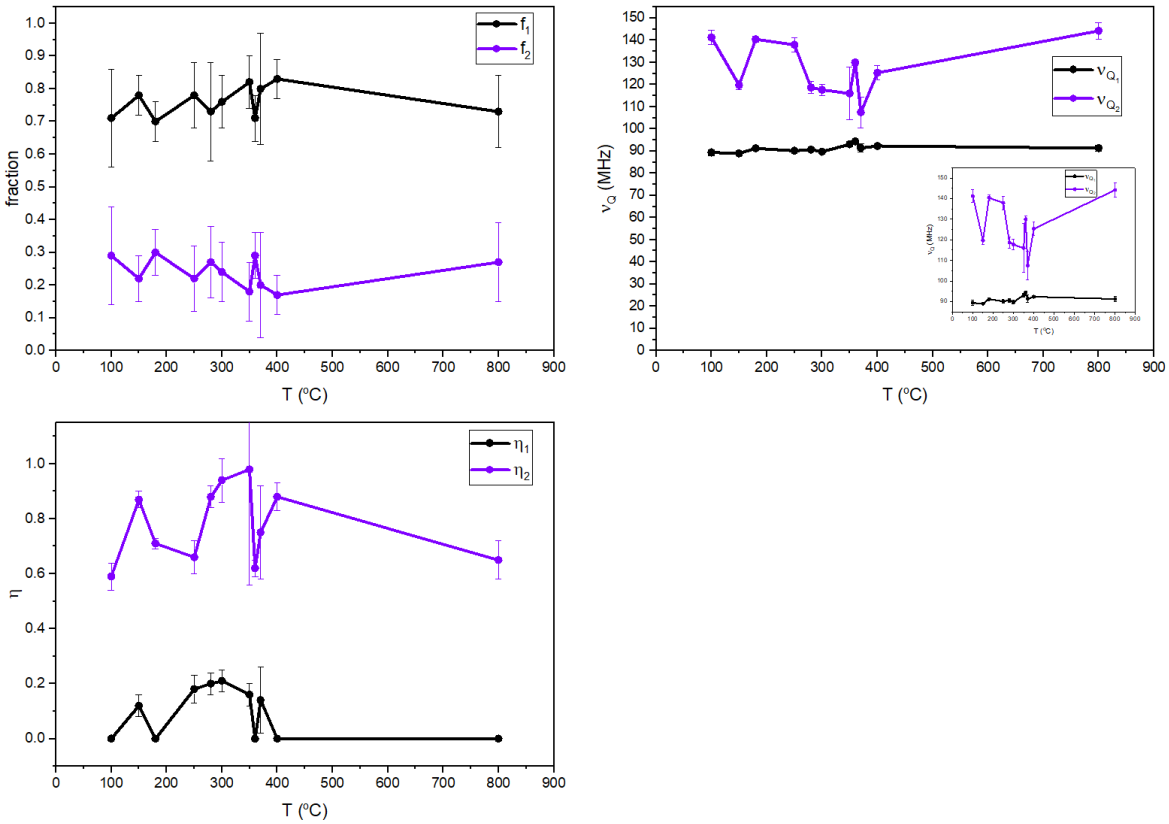

Fig. 17. Curves of hyperfine interaction parameters for two fractions

5.3.3 Comparison between non-compressed and compressed data

Some compressed R(t) spectra data don't provide good fittings because the smoothed algorithm for data compression reduces the number of data points and increases the time per channel, i. e. the algorithm can remove both unnecessary, false data points and important data points. And that is why such a fit won't be very high quality and accurate, and therefore the determination of the parameters of hyperfine interaction will also not be very high quality. In the concept of these experimental data, the uncompressed data gives better fitting spectra than the compressed ones. However, in other cases when the time per channel is quite small leading to the "condensed" R(t) spectra, the compressed data is essential.

CHAPTER 6: Conclusion

In this work, we use TDPAC measurements to investigate the local environment around an implanted ^{111m}Cd (^{111}Cd) nuclear probe in Bismuth Ferrite. The TDPAC measurements were obtained at different temperatures (15 - 500^{o}C) from two TDPAC spectrometers: an analog 4-detector setup (K1) and a digital 6-detector setup (KATAME). The experimental results agree well with calculations based on TDPAC theory. The substitutional Bi site location of the ^{111m}Cd (^{111}Cd) probe is confirmed using ab-initio DFT simulations.[2] The results of the R(t) spectra show that the electric frequency is almost stable and doesn't depend on temperature. This is due to the implantation of the Cd^{2+} ion instead of the Bi^{3+} ion, which leads to a decrease in the lattice parameter and the volume of the unit cell. Since the radius of the Cd^{2+} ion (0.095 nm) is smaller than the radius of the Bi^{3+} ion (0.103 nm), the structure of $BiFeO_3$ is distorted from rhombohedral to orthorhombic. Therefore, the orthorhombic structure is more stable than the original rhombohedral structure of $BiFeO_3$. The replacement of Bi^{3+} with Cd^{2+} leads to a change of Fe^{3+} to Fe^{4+} in the compound to compensate for the unbalanced charge, which in turn means that the magnetic moment will be close to zero for Fe^{4+} ions, and hence no magnetic frequency will be observed. The existence of Fe^{4+} in the unit cell shown in Fig. 2, will disrupt the super exchange interaction between Fe^{3+}-Fe^{3+}, which is known as the main mechanism leading to the antiferromagnetic order in bismuth ferrite.

Acknowledgements

We thank the support received from the Federal Ministry of Education and Research (BMBF) under grants 05K16PGA, 05K22PGA and 05K22PGB. We also thank the European Union's Horizon Europe Framework research and innovation programme under grant agreement no. 101057511 (EURO-LABS).

Also, special thanks to my supervisors Dr. Juliana Schell, ISOLDE Solid State Physics Coordinator and Thien Thanh Dang, from the Institute for Materials Science and Center for Nanointegration Duisburg-Essen (CENIDE), University of Duisburg-Essen, for the opportunity to be part of this work.

References

[1] G. Catalan and J. F. Scott, Physics and applications of bismuth ferrite, Adv. Mater. 21, 2463 (2009).

[2] G. Marschick, J. Schell, B. Stöger, J. N. Gonçalves, M. O. Karabasov, D. Zyabkin, A. Welker, M. Escobar C., D. Gaertner, I. Efe et al., Multiferroic bismuth ferrite: perturbed angular correlation studies on its ferroic α-β phase transition, Phys. Rev. B 102, 224110 (2020), DOI: https://doi.org/10.1103/PhysRevB.102.224110.

[3] Dang, T. T.; Schell, J.; Boa, A. G.; Lewin, D.; Marschick, G.; Dubey, A.; Castillo, M. E.; Noll, C.; Beck, R.; Zyabkin, D.; Glukhov, D.; Yap, I. C. J.; Mokhles Gerami, A.; Lupascu, D. C. Temperature dependence of the local electromagnetic field at the Fe site in multiferroic bismuth ferrite. Phys. Rev. B 2022, 102, 054416.

[4] Wikipedia article on Multiferroics,
URL:https://en.wikipedia.org/wiki/Multiferroics

[5] Wikipedia article on Perovskite (structure),
URL:https://en.wikipedia.org/wiki/Perovskite_(structure)

[6] D. C. Arnold, K. S. Knight, F. D. Morrison, and P. Lightfoot, Ferroelectric-Paraelectric Transition in $BiFeO_3$: Crystal Structure of the Orthorhombic β Phase, Phys. Rev. Lett. 102, 027602 (2009).

[7] S. R. Burns, O. Paull, J. Juraszek, V. Nagarajan, and D. Sando, The experimentalist's guide to the cycloid, or noncollinear antiferromagnetism in epitaxial $BiFeO_3$, Adv. Mater. 32, 2003711 (2020).

[8] J. B. Neaton, C. Ederer, U. V. Waghmare, N. A. Spaldin, and K. M. Rabe, First-principles study of spontaneous polarization in multiferroic $BiFeO_3$, Phys. Rev. B 71, 014113 (2005).

[9] Schell, J.; Schmuck, M.; Efe, İ.; Dang, T. T.; Gonçalves, J. N.; Lewin, D.; Castillo, M. E.; Shvartsman, V. V.; Granadeiro Costa, A. R.; Köster, U.; Vianden, R.; Noll, C.; Lupascu, D. C. Strong magnetoelectric coupling at an atomic nonmagnetic electromagnetic probe in bismuth ferrite. Phys. Rev. B 2022, 105, 094102.

[10] T. Wichert and E. Recknagel, Microscopic Methods in Metals (Springer, New York, 1986), pp. 317–364.

[11] J. Schell, P. Schaaf, and D. C. Lupascu, Perturbed angular correlations at ISOLDE: A 40 years young technique, AIP Adv. 7, 105017 (2017), DOI: https://doi.org/10.1063/1.4994249.

[12] R. Nédélec, Rückstoßimplantation von 48Cr und erste PAC Messungen mit der Sonde 48Cr/48V, Ph.D. thesis, Diplomarbeit, Universität Bonn, 2002.

[13] G. Schatz and A. Weidinger, Nuclear Condensed Matter Physics: Nuclear Methods and Applications (Wiley, Chichester, 1996).

[14] E. Danielsen, R. Bauer, L. Hemmingsen, M.-L. Andersen, M. J. Bjerrum, T. Butz, W. Troger, G. W. Canters, C. W. G. Hoitink, G. Karlsson et al., Structure of metal site in azurin, Met^{121} mutants of Azurin, and stellacyanin investigated by ^{111m}Cd perturbed angular correlation (PAC), J. Biol. Chem. 270, 573 (1995).

[15] A. Abragam and R. V. Pound, Physical Review 92, 943 (1953).

[16] H. Frauenfelder, R. M. Steffen, and K Siegbahn, α-, β- and γ-Ray Spectroscopy, edited by K. Siegbahn (North-Holland, 1965).

[17] R. Catherall, W. Andreazza, M. Breitenfeldt, A. Dorsival, G. J. Focker, T. P. Gharsa, T. J. Giles, J-L. Grenard, F. Locci, P. Martins et al., The ISOLDE facility, J. Phys. G: Nucl. Part. Phys. 44, 094002 (2017).

[18] K. Johnston, J. Schell, J. G. Correia, M. Deicher, H. P. Gunnlaugsson, A. S. Fenta, E. David-Bosne, A. R. G. Costa, and D. C. Lupascu, J. of Phys. G: Nucl. Particle Phys. 44, 104001 (2017)

[19] Schell J. Alternative Approaches to Study Mining and Mineral Science at ISOLDE-CERN, Aspects Min. Miner. Sci. 2020, 4(4). https://doi.org/10.31031/AMMS.2020.04.000592.

[20] IAEA Table of Nuclides: https://www-nds.iaea.org/relnsd/vcharthtml/VChartHTML.html

[21] M. Nagl, U. Vetter, M. Uhrmacher, and H. Hofsäss, A new alldigital time differential γ-γ angular correlation spectrometer, Rev. Sci. Instrum. 81, 073501 (2010).

[22] Tilman Butz. “Fourier Transformation for Pedestrians”, Second Edition, 2015. Chapter 5, p. 147, Data Compression.

[23] R. D. Shannon, Revised effective ionic radii and systematic studies of interatomic distances in halides and chalcogenides, Acta Cryst. A 32, 751 (1976).

[24] Goncalves et al., Journal of Materials Science: Materials in Electronics volume 29, pages 784–793 (2018); DOI 10.1007/s10854-017-7973-4.

[25] Graf et al 2018 J. Phys.: Condens. Matter 30 285701; DOI 10.1088/1361-648X/aac74f.

[26] Chao et al., J. Mater. Chem. A, 2019, 7, 12176; https://doi.org/10.1039/C9TA02569C.

[27] Coupled electrical and magnetic properties in (La, Sr)FeO_{3-} δ, JOURNAL OF APPLIED PHYSICS 97, 10C314 s2005d, DOI: 10.1063/1.1860911.